Journal of Hydrology 583 (2020) 124558

Contents lists available at ScienceDirect

Journal of Hydrology

journal homepage: www.elsevier.com/locate/jhydrol

Research papers

High-resolution characterization of nanoparticle transport in heterogeneous porous media *via* low-field nuclear magnetic resonance

Qian Zhang[a,b,c], Yanhui Dong[a,b,c,*], Hang Deng[d], Derek Elsworth[e]

[a] Key Laboratory of Shale Gas and Geoengineering, Institute of Geology and Geophysics, Chinese Academy of Sciences, Beijing 100029, China
[b] University of Chinese Academy of Sciences, Beijing 100049, China
[c] Innovation Academy for Earth Science, Chinese Academy of Sciences, Beijing 100029, China
[d] Energy Geosciences Division, Earth and Environmental Sciences Area, Lawrence Berkeley National Laboratory, Berkeley, CA, USA
[e] Department of Energy and Mineral Engineering, G^3 Center and EMS Energy Institute, The Pennsylvania State University, University Park, PA 16802, USA

ARTICLE INFO

This manuscript was handled by Huaming Guo, Editor-in-Chief, with the assistance of XXX, Associate Editor

Keywords:
Nanoparticle transport
Porous media
Low-field nuclear magnetic resonance
Heterogeneity

ABSTRACT

Understanding the transport of nanoparticles (NPs), including nanoscale zero-valent iron (nZVI) particles, through water-saturated porous media has important implications for many natural and engineered systems. For the first time, we use spin-echo single point imaging (SE-SPI) of low-field Nuclear Magnetic Resonance (LF-NMR) to monitor nanoparticle transport through a heterogeneous porous medium. The ability of this method to provide information of nano- to micro-scale pore structure and to monitor transient processes is verified by a transport experiment using modified nZVI particles. Early breakthrough of the NP front and large amount of residual NPs (27% of the iron was retained in the core) were observed in the experiment. These observations were due to the presence of preferential flow paths and dead-end pores as demonstrated by micro X-ray Computed Tomography (μCT) imaging. Spatial and temporal data provided by this method enabled numerical simulations to quantify the impacts of spatial heterogeneity in pore structure on NP transport in terms of transport parameters. The simulation that captures the spatial heterogeneity by explicitly considering four regions of distinct porosities outperforms the model assuming a homogeneous pore structure. The maximum of residual sum of squares reduced from 0.328 to 0.138 when considering the impact of pore structure. The transport parameters vary significantly among different regions. For example, in the lowest porosity region of this sandstone, colloid dispersion (*D*) is 0.10 cm^2/min instead of 0.20 cm^2/min in the most connected region, while the attachment (k_{ac}) increased from 0.007 to 0.025 min^{-1}. Overall, SE-SPI imaging is shown to be an important tool in refining transport processes of NPs in heterogeneous porous media with application to constrain complex natural systems.

1. Introduction

Nanoparticles (NPs), especially nanoscale zero-valent iron (nZVI) particles, have been extensively used for direct treatment of contaminated zones in aquifers because of their desirable properties, i.e. high specific surface area and potential mobility (Zhang, 2003; Kanel et al., 2006; Kocur et al., 2013). The remediation efficiency and environmental safety of the application of NPs are controlled by their mobility in porous media (Karn et al., 2009; Hosseini et al., 2011; O'Carroll et al., 2013). Bare nZVI particles are subject to rapid aggregation and settling (Phenrat et al., 2007; Tiraferri et al., 2008), and thus are typically modified by adding polymers, anionic surfactants, as well as incorporating solid matrices (Tiraferri and Sethi, 2009; He et al., 2010; Zhao et al., 2016; Fajardo et al., 2019). However, cell membranes disruption, chlorosis or hypoxia have been observed upon exposure to modified NPs (Saif et al., 2016; Yoon et al., 2018), indicating potential adverse health impacts on microbes, plants and human. Therefore, it is important to understand and predict the transport and the fate of modified NPs in aquifers, which are largely influenced by the structure and transport properties of the porous media.

Experimental studies used to investigate the transport properties of NPs in porous media typically involve monitoring NP concentrations only at the outlet of packed columns. The interior processes are then inferred using empirical relations such as colloid filtration theory (CFT) (Kim et al., 2007; Vecchia et al., 2009; Phenrat et al., 2009). This type of breakthrough curve analysis, although informative, provides limited insights regarding the spatial heterogeneity of the column, which has a considerable impact on NPs transport, retardation and attenuation.

* Corresponding author.
E-mail address: dongyh@mail.iggcas.ac.cn (Y. Dong).

https://doi.org/10.1016/j.jhydrol.2020.124558
Received 25 March 2019; Received in revised form 22 November 2019; Accepted 8 January 2020
Available online 01 February 2020

Recently, a range of non-invasive techniques, including optical imaging, gamma radiation, micro X-ray Computed Tomography (μCT) imaging, and nuclear magnetic resonance (NMR), have been used to characterize the spatial distribution of NPs in porous media (Werth et al., 2010) and to resolve local transport processes. For example, optical imaging has been used to track the spatial distribution of fluorescent or color tracers as they flow through a model porous medium (Zinn et al., 2004; Willingham et al., 2008). But the application is limited to translucent media, and typically two-dimension systems (Werth et al., 2010). While gamma radiation and μCT are powerful tools for the characterization of complex pore structures and for saturation imaging of one or more fluids (Turner et al., 2004; Nizovtsev et al., 2008; Peng et al., 2012), the relatively long counting time at a single location limits their application for intrinsically transient phenomena such as fluid flow and particle transport.

NMR is another promising non-invasive imaging technique, which quantifies nuclear spin or rotation of elementary particles (e.g. ^{1}H nuclei). Compared to other imaging techniques, the NMR signal is dominated by the liquid phase and does not require phase segmentation. In addition, NMR allows a wide range of temporal and spatial resolutions. NMR techniques, especially magnetic resonance imaging (MRI), have been increasingly used in contaminant hydrology to evaluate NP transport processes and quantify transport properties of NPs in saturated geo-materials (Ramanan et al., 2011; Bray et al., 2017; Lehoux et al., 2017). For example, Lakshmanan et al. (2015) reconstructed the evolving NPs concentrations in the packed columns of quartz and dolomite gravel from MRI images and evaluated the transport parameters and interaction energy profiles using the CXTFIT software package and Derjaguin-Landau-Verwey-Overbeek (DLVO) theory.

Most MRI studies use high-field instruments to acquire relatively high spatial resolution, on the order of ~mm to 100 μm (Werth et al., 2010). But it is still inadequate for fine-grained media (pore diameter < 600 μm) (Lakshmanan et al., 2015; Bray et al., 2017). In addition, high-field imaging has the issue of pore-scale magnetic field distortions (so-called “internal gradients”), when the materials are heterogeneous. As a result of such distortions, the decay of transverse magnetization with respect to molecular diffusion is enhanced and concentrations are typically under-estimated. As such, the use of high-field imaging in the investigations of NPs transport in geo-materials is limited (Mitchell and Fordham, 2015).

Low-field nuclear magnetic resonance (LF-NMR) spectrometers provides a better alternative for laboratory investigations of NP transport in porous media that are comparable to natural aquifers (Mitchell et al., 2010). LF-NMR is less affected by internal gradients, enabling quantitative analysis. In addition, the spin-echo single point imaging (SE-SPI) method of low-field NMR has the ability to monitor transient processes in heterogeneous porous media. First, the SE-SPI sequence allows the imaging of NP transport through consolidated porous materials with nano-scale pores. It obtains transverse relaxation time (T_2) distribution profiles with phase-encoded MRI. Every T_2 curve contains encoded information of pore structure spanning nano- to micro-scale for the specific profile. Second, the rapid loss of the transverse time resulting from the presence of paramagnetic NPs can be detected by the SE-SPI sequence on a time scale of seconds and thus enables dynamic monitoring of transient processes (Petrov et al., 2011). Moreover, using multi-profile concentration data converted from NMR data, the SE-SPI sequence provides non-invasive observations of NP transport processes at different locations.

We explore the use of low-field NMR to monitor transport behaviors of NPs in consolidated porous media and demonstrate how this contributes to an improved understanding of the impacts of spatial heterogeneity on mass transport. This is among the first efforts to apply SE-SPI low-field NMR imaging in investigating transport processes of NPs typically used in environmental remediation. We use modified nZVI (Jia et al., 2011) as a candidate particle in spatially heterogeneous porous media commonly encountered in natural aquifers. Spatial histories of concentration are recovered from the NMR measurements. Complementary simulations, informed by these experimental observations, highlight the impact of spatial heterogeneity on transport processes with μCT imaging corroborating the inverted pore structure.

The paper is organized as follows. In Section 2, we introduce the materials, experimental methods, and the governing equations used in the simulations. The results of the calibration tests and transport experiments are described in Section 3. In Section 4, we discuss the impacts of spatial heterogeneity on NPs transport as observed in experiments based on complementary simulations. We close with a few concluding remarks.

2. Materials and methods

2.1. Nanoparticles

The modified nZVI particles used in the experiments consist of smectite clay templates and subnano-sized zero-valent in the interlayers, and the iron content is ~4% by weight (Gu et al., 2010). The size of the elementary platelets of the smectites range from tens to hundreds of nanometers with an average of ~60 nm, and determines the diameters of the colloids in the suspensions. The suspensions were prepared by mixing the modified NPs with deionized water, and centrifuged to ensure homogeneity. The NPs are stable in the suspensions, because the structure of the clay templates prevents direct contact between Fe^0 clusters and thus agglomeration of the nZVI particles (Jia and Wang, 2013). This is confirmed by the batch tests, in which the suspensions were left in experimental vials and remained homogeneous for up to two days, much longer than the time scale of the flow-through experiment. As such, the experimentally observed NP transport can be attributed to the transport properties of the porous media, instead of potential aggregation and deposition associated with particle surface properties.

Twelve suspensions were prepared for the concentration calibration tests. The iron concentrations of the prepared suspensions range from 0.0005 to 0.1430 mM, and were confirmed by inductively coupled plasma mass spectrometry (ICP-MS) measurements.

2.2. Porous media

Six homogeneous packed columns were prepared for the calibration tests. The quartz sands used were first soaked in concentrated HCl (12 mol/L) for 12 h and rinsed in deionized water. Each column is 25 mm in diameter and 25 mm long, and is packed with quartz sands following the face-centered cubic (FCC) packing procedure. The six quartz sand columns have grain sizes (S1 to S6) of 105, 125, 149, 165, 250, and 425 μm, respectively. The corresponding pore sizes are 16.275, 19.375, 23.095, 25.575, 38.750, and 65.875 μm, according to the empirical relation between the pore size (d_p) and the grain size (D_g) for the FCC array (d_p = 0.155 Dg).

An artificial sandstone core with a diameter of 24.95 mm and a length of 50.15 mm was used in the transport experiment. Chemically modified epoxy resin with triethanolamine (TEA) was used to bind together quartz sands with sizes from 125 to 149 μm to create the hydrophilic artificial sandstone core (Xie et al., 2016). The core has a gas permeability of 100 mD representing the lower range of typical aquifer permeabilities. More details of the core properties, including imaging by μCT and characteristics of the pore structure are discussed in Section 4. Prior to the experiment, the core was dried at 105 °C for 24 h with a vacuum applied to 0.1 Pa absolute for 3 h before saturating with water at 5 MPa for 12 h.

2.3. Test procedures and experimental apparatus

Two sets of calibration tests were performed to establish the method of quantifying iron concentration profiles from NMR data. The first set

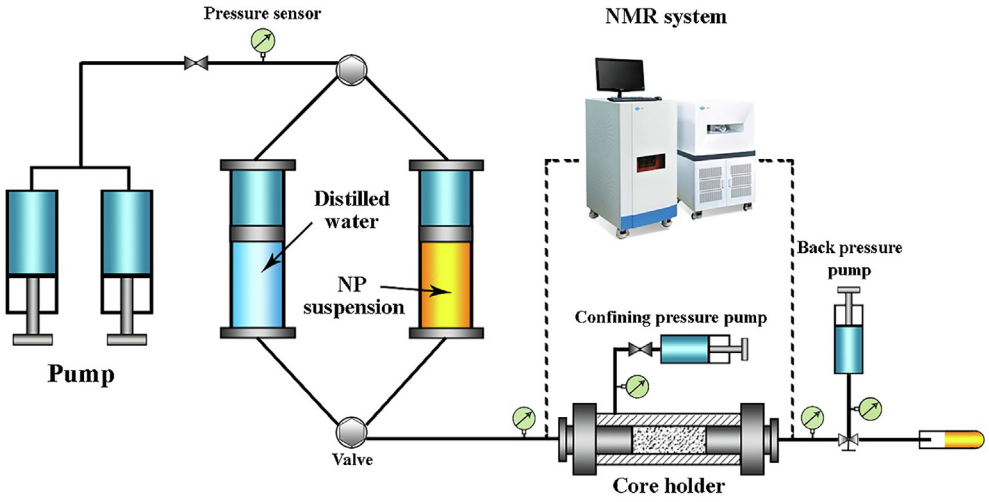

Fig. 1. Schematic illustration of the core displacement system.

of tests was performed on twelve suspensions of different iron concentrations to build the relationship between iron concentrations and NMR signals. Then, packed columns of different grain sizes saturated with suspensions were tested to examine the impacts of pore structure on T_2 relaxation times.

For the transport experiment, the sandstone core was placed horizontally into a core displacement system with a nonmagnetic core holder (Fig. 1) and was first flushed with deionized water to remove the air and establish steady state flow. T_2 data were collected before the transport experiment, serving as a reference. Fluid flow was then established at a constant flow rate of 0.1 mL/min. For the first 55 mins of the transport experiment, the inflow was a suspension of NPs at a concentration of 0.1 g/L, corresponding to an iron concentration of 0.07 mM in the suspension. The inflow was subsequently switched to deionized water with the entire experiment lasting 120 mins with NMR measurements collected every 5 mins.

NMR measurements were performed on a Niumag system, which includes a 0.5 T superconducting magnet with a resonant frequency of 21 MHz and a 60-mm probe. The experiments were performed with the following parameters: an echo time (TE) of 0.025 ms, a repetition time (TR) of 3000 ms, and 16 scans (NS). In the calibration tests, T_2 relaxation times were obtained using the SE-SPI sequence with one slice enclosing the entire sample. In the NP transport test, SE-SPI sequence data were collected at 15 locations evenly distributed along the core - from inlet to outlet. CT images of the sandstone core were collected to characterize the pore structure using a Zeiss Xradia scanner (520 Versa) at 80 KV and 87 μA. The resulting image resolution is approximately $26 \times 26 \times 26$ μm^3. The three-dimensional pore structure of the sandstone was analyzed using Avizo visualization software.

2.4. Quantitative measurement of NP concentrations

The local magnetic field fluctuations of the paramagnetic NPs result in rapid loss of the transverse magnetization and thus shorter T_2 times relative to those for pure water (Pykett et al., 1982). The shortening of relaxation rates per unit concentration of NPs is defined as the relaxivity (R) (Caravan et al., 1999), and has a unit of $mM^{-1}s^{-1}$. The relaxivity is generally dependent on the strength of the magnetic field. The concentration of paramagnetic NPs, [C], is related to the transverse relaxation time of pure water as follows (Bloembergen and Morgan, 1961; Strijkers et al., 2007):

$$[C] = \frac{1}{R}\left[\frac{1}{T_{2,i}} - \frac{1}{T_{2,0}}\right] \tag{1}$$

where $T_{2,0}$ is the relaxation time in the absence of paramagnetic NPs, and $T_{2,i}$ is the relaxation time in the presence of a concentration [C] of paramagnetic NPs.

The influence of the porous medium on T_2 may be examined in terms of the transverse relaxation rate $1/T_2$ that comprises the bulk, surface, and enhanced diffusion relaxation rates (Behroozmand et al., 2014):

$$\frac{1}{T_2} = \frac{1}{T_{2B}} + \rho_0\frac{S}{V} + \frac{D_m(GT_E\gamma)^2}{12} \tag{2}$$

where T_{2B} is the bulk relaxation time, ρ_0 is the transverse surface relaxation strength, S is the pore surface area, V is the pore volume, D_m is the molecular diffusion coefficient, G is the magnetic field gradient, T_E is the echo spacing, and γ is the gyromagnetic ratio. Given that the bulk relaxation is slower than the surface relaxation then the small magnetic field gradient, Eq. (2) can be simplified as follows:

$$\frac{1}{T_2} \approx \rho_0\frac{S}{V} \tag{3}$$

Eq. (3) was verified by calibration tests on packed quartz sand columns of different grain sizes. In addition, the effect of the paramagnetic NP concentration on T_2 in two different pore structures was also evaluated prior to the transport experiment using Eqs. (1) and (2).

2.5. Estimation of transport parameters

The transport parameters were evaluated using the HYDRUS-1D software package which accommodates key processes associated with colloid transport in variably saturated porous media (Šimůnek et al., 2006). The transport and fate of colloids is accommodated by the advection–dispersion equation that is modified to account for colloid filtration. In the absence of colloid inactivation and degradation, processes not anticipated in our experiment, the colloid transport equation is given as:

$$\frac{\partial\theta C_c}{\partial t} + \rho\frac{\partial S_c}{\partial t} = \frac{\partial}{\partial x}\left(\theta D\frac{\partial C_c}{\partial x}\right) - \frac{\partial qC_c}{\partial x} \tag{4}$$

where C_c is the colloid concentration in the aqueous phase (nL^{-3}), S_c is the solid phase colloid concentration (nM^{-1}), θ is the volumetric water content (L^3L^{-3}), D is the dispersion coefficient for colloids (L^2T^{-1}), and q is the volumetric water flux density (LT^{-1}), t is the time and x is the distance to the injection point. The colloid mass transfer term between the aqueous and solid phases is traditionally given as:

$$\rho\frac{\partial S_c}{\partial t} = \theta k_{ac}\psi_s C_c - \rho k_{dc}S_c, \tag{5}$$

where k_{ac} and k_{dc} are first-order colloid attachment and detachment coefficients (T^{-1}), respectively, and ψ_s is a dimensionless colloid retention function. In this study, D, k_{ac} and k_{dc} are the key parameters representing transport and were evaluated by inverse solution using HYDRUS-1D with porosity and permeability treated as the known parameters.

The NPs were delivered as a pulse input from the inlet. The corresponding initial and boundary conditions are:

$$C(x, t = 0) = 0$$
$$C(x = 0, 0 < t < t_i) = C_0$$
$$C(x = 0, t > t_1) = 0$$
$$\frac{dC}{dx}\Big|_{x=L} = 0 \quad (6)$$

where t_1 is the pulse input time, and L is the length of the sandstone.

3. Results

3.1. Calibration for relaxivity constant

The first set of calibration tests obtained the relaxivity constant of modified nZVI particles, mentioned in Eq. (1), to establish the quantitative measurement of NP concentrations. Fig. 2 shows that the transverse relaxation rate $[1/T_{2,i}–1/T_{2,0}]$ follows a linear relationship with respect to the concentration of the NPs where T_2 was measured three times for each NP suspension. The percentage errors for the individual T_2 measurements are between 0.17% and 0.46%, corresponding to percentage errors of 0.22% to 2.11% for $[1/T_{2,i}–1/T_{2,0}]$. The small measurement errors (not visible on the figure) and high repeatability confirmed the stability and reliability of the method. The relaxivity constant R of the modified nZVI particles determined using the least squares fit method is 86.63 $mM^{-1}s^{-1}$, with goodness-of-fit coefficient (R^2) larger than 0.99.

3.2. Effects on NMR signals in porous media

To quantify the impacts of the pore structure on T_2 relaxation, T_2 tests were also performed on six columns packed with quartz sands of different sizes (S1 to S6) using NP suspensions of the same iron concentration of 0.05 mM. The results (Fig. 3a) show that $\frac{1}{T_2}$ increases linearly with $\frac{S}{V}$, where the S and V were calculated using pore sizes. The high goodness-of-fit also verifies that Eq. (3) provides a reasonable mathematical description of the impacts of pore structure on T_2 relaxation.

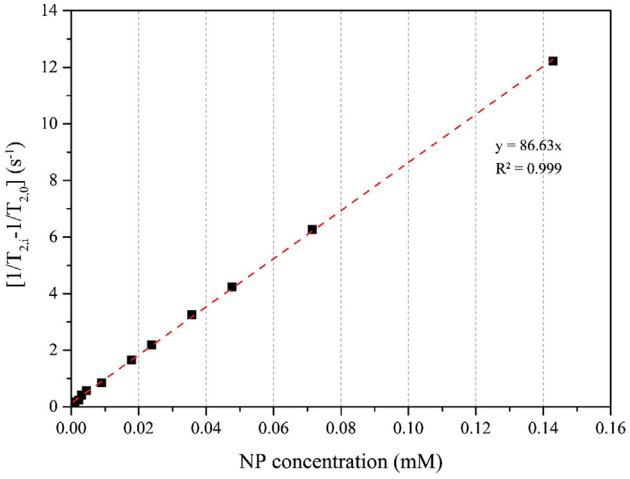

Fig. 2. Variation in the change of the transverse relaxation rate $[1/T_{2,i}–1/T_{2,0}]$ with respect to NP concentration (iron concentrations of the modified nZVI in suspension).

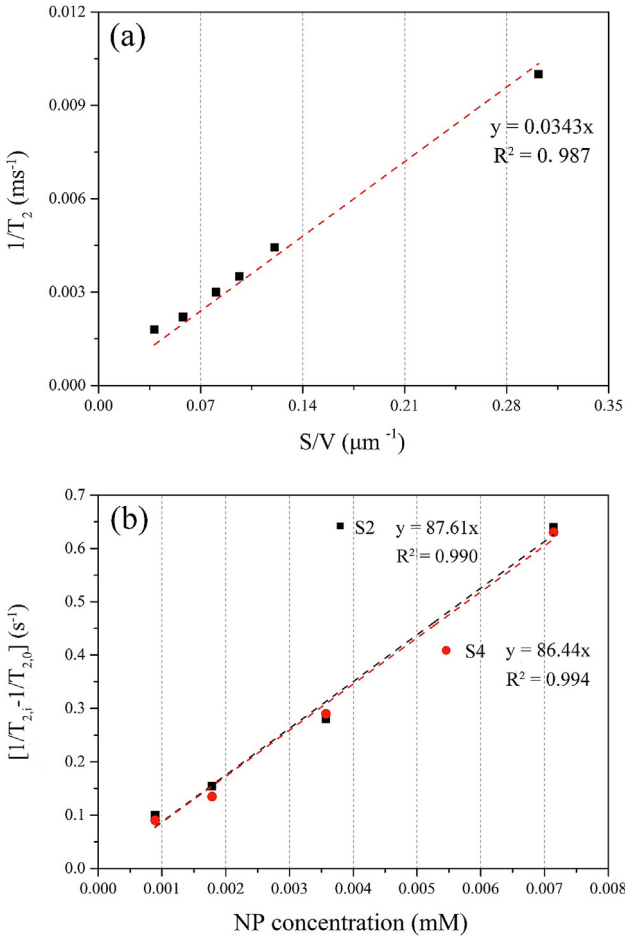

Fig. 3. Variation in the change of the transverse relaxation rate with respect to (a) S/V (Six different pore sizes of quartz sands were used as porous media for the different S/V values), and (b) the NP concentrations (iron concentrations of the modified nZVI in suspension) in different porous media (S2, S4).

Although pore structure largely affects the magnitudes of the T_2 relaxation, their impacts on transverse relaxation rate is minimal. The relationships between the transverse relaxation rate and the iron concentration measured in two packed columns (S2 and S4) are similar (Fig. 3b). The fitted values of R based on Eq. (1) are 87.61 $mM^{-1}s^{-1}$ and 86.44 $mM^{-1}s^{-1}$, respectively, and are comparable to the values derived from the calibration tests that were performed without porous media (Fig. 2).

Collectively, the observations confirm that the impacts of concentration and pore structure on T_2 relaxation are independent of each other, and can be accounted for by the relaxivity R and the ratio of pore surface to volume ratio $\frac{S}{V}$, respectively. Since $\frac{S}{V}$ is included in the calculation of $T_{2,0}$, the relationship between the transverse relaxation rate is only dependent on concentration. This relationship allows the deciphering of the paramagnetic NP transport processes using T_2 measurements in heterogeneous porous media.

3.3. NMR measurements of NP transport in sandstone

Transport of the modified nZVI particles through the sandstone core was also monitored using the SE-SPI sequences. The relaxivity constant R for the modified nZVI particles in the sandstone core was derived following the same procedure described above. A value of 86.41 $mM^{-1}s^{-1}$ was obtained and used to convert NMR measurements into concentration data in the transport experiments using the same sandstone core. The T_2 data were collected along the core at an interval

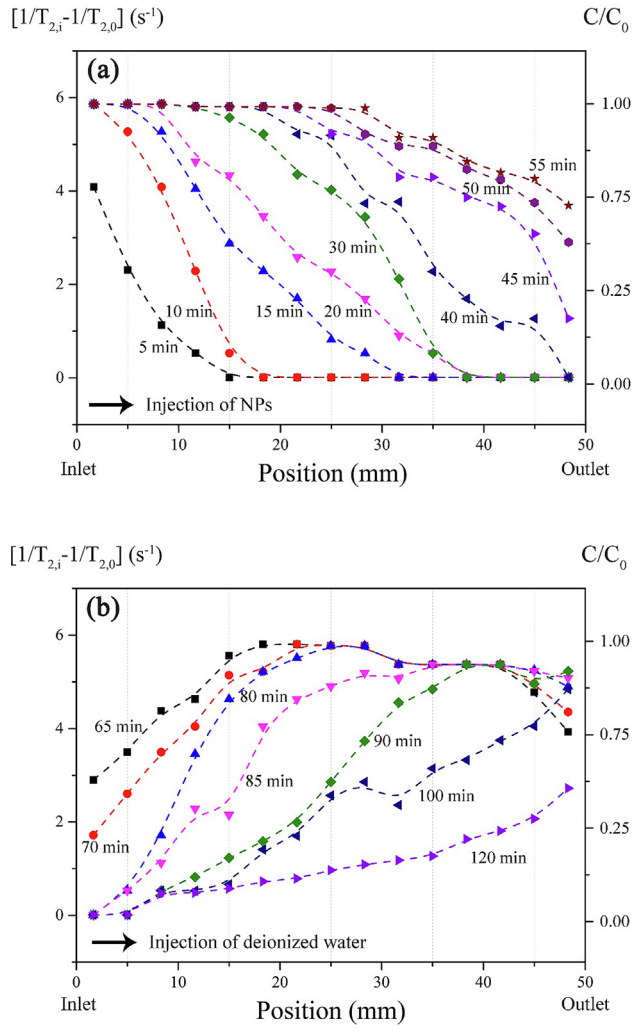

Fig. 4. Data of transverse relaxation rate ($[1/T_{2,i}–1/T_{2,0}]$, left Y-axis) and relative concentration (C/C_0, right Y-axis) at different time intervals to constraine NP transport processes in the sandstone. (a) 0–55 mins, the continuous injection of NPs; (b) 65–120 mins, the continuous injection of deionized water (higher magnitudes of $[1/T_{2,i}–1/T_{2,0}]$ scale with higher iron concentrations).

of 3.33 mm every five minutes. The transverse relaxation rate is directly related to iron concentration (see Section 3.1) and is recorded along the core sample at successive time intervals as shown in Fig. 4. This defines the variation of relative concentrations C/C_0 (C is the measured concentration of iron, and C_0 is the influent iron concentration) along the sandstone resulting from the transport of the modified nZVI particles.

During the injection of NPs (0–55 min), the values of $[1/T_{2,i}–1/T_{2,0}]$ gradually increase along the core as the concentration front advances from the inlet to the outlet. The front where the NPs were first detected migrates much faster than the bulk transport of the NPs (e.g. at 15 and 20 mins), potentially indicating the presence of preferential flow paths. At the conclusion of the injection (55 min), a large portion of the sandstone was saturated by the NP suspension, as indicated by the uniform distribution of large $[1/T_{2,i}–1/T_{2,0}]$ magnitudes. Although NPs were detected at the outlet at 40 mins, the bulk of the NPs did not break through the core by the end of the injection - as confirmed by the relatively low $[1/T_{2,i}–1/T_{2,0}]$ values occupying the final 15 mm of the core length. This may be attributed to both the attachment of NPs to the sandstone grains and the innate complexity of the pore structure.

During the injection of deionized water (55–120 min), $[1/T_{2,i}–1/T_{2,0}]$ magnitudes first decrease close to the inlet and increase close to the outlet as the prior concentration distribution is displaced along the core, effectively flushing-out of the NPs. However, at the conclusion of the injection of the DI water the $[1/T_{2,i}–1/T_{2,0}]$ values do not return to zero - indicating the presence of residual NPs in the aqueous phase or attached to grains. The residual NPs may represent trapping in poorly connected pores or mechanical/electrostatic trapping on grain boundaries and their continuous detachment of NPs from the sandstone. Supplementary characterization methods are necessary to fully deconvolve other mechanisms for the trapping of residual NPs.

Fig. 5 provides a visualization of the pore structures reconstructed from the μCT images with the pore space color-coded by the relative concentration C/C_0. The peak value of iron concentration measured by the C/C_0 ratio decreased from 0.98 to 0.87, which indicates an increase in NP retention over time. The iron recovery, which measures the ratio between the amount of iron collected at the outlet and the amount of iron injected into the core, was calculated from the ICP measurements of the effluent samples and is 73% - identifying net retention of NPs in the sandstone core. There was, however, no observable clogging phenomenon since there was no detectable change in the pressure drop between the inlet and outlet. This is also consistent with the observation that the modified nZVI particles are unlikely to aggregate (Jia and Wang, 2013).

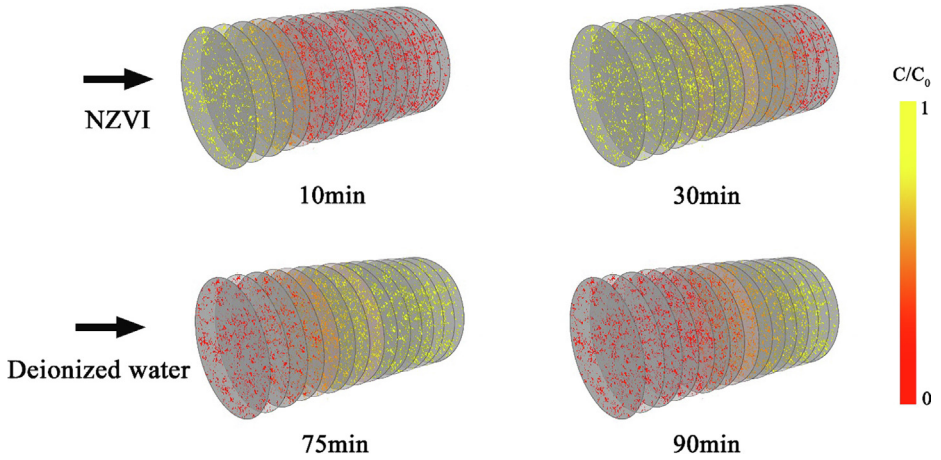

Fig. 5. Spatial distribution of the NPs in the three-dimensional sandstone structure at selected time intervals with C/C_0 representing the concentration of iron (C) relative to the inlet solution (C_0). An inlet suspension of NPs was injected from 0 to 55 mins, with deionized water injected from 55 to 120 mins.

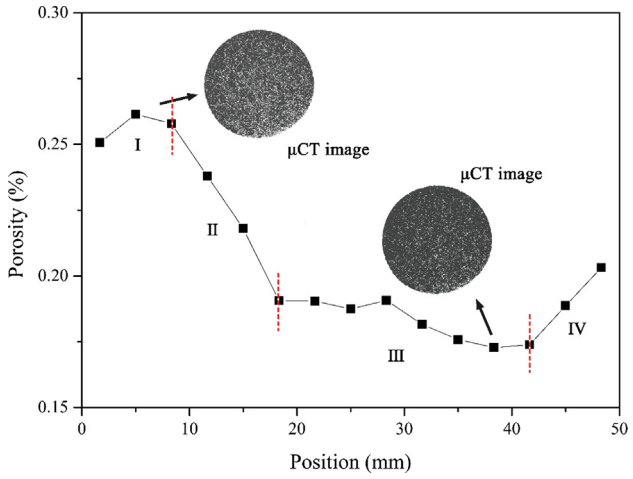

Fig. 6. Connected porosity for 15 slices along the sandstone (The μCT images show the difference of connected porosity for each slice. Four distinct regions (I–IV) are defined, based on porosities).

4. Discussion

In this section, we discuss the impacts of pore structure heterogeneity, as confirmed by the μCT images, on the transport of NPs, by comparing transport parameters obtained using two sets of simulations with different assumptions of the pore structure.

The spatial heterogeneity of the three-dimensional structure of the sandstone was confirmed by μCT imaging. Pores within the sandstone were distributed with an average diameter of ~35 μm. Binarization of the μCT images recovers an average porosity of ~0.203, which is close to the ratio of the volumes of the aqueous phase to the core. However, the connected porosity varies spatially along the core with four distinct regions observed (Fig. 6). Region I has the highest connected porosity, and region III (from slice 6 to slice 13) the lowest.

Spatial heterogeneity of the pore structure, i.e. the presence of well-connected flow paths and poorly connected pores or dead-end pores, as inferred from the experimental concentration data, is further highlighted in Fig. 7. Connectivity analysis and skeletonization were performed using Avizo to define the 3D digital structure of the sandstone. The skeletonization module extracts the centerlines of interconnected pore regions and calculates a distance map that measures the distance of a voxel in the pore space to the nearest solid phase from the segmented images. The 3D skeleton consists of nodes and tubes and defines the topology. The nodes are the branching points and endpoints, connected by the tubes, whose thickness depends on the maximum value on the distance map. Dead-end pores are highlighted (orange dotted circles in Fig. 7b) with the prescribed network allowing flow calculations on a subsection of the sample (Avizo XLab Hydro module). Streamlines (see Fig. 7c) show the relative velocity field with red defining the higher velocity preferential flow paths that likely act as fast channels for NP transport.

HYDRUS-1D was used to simulate flow, using the experimental observations of concentration history to invert for the transport parameters: dispersion coefficient D, attachment coefficient k_{ac} and detachment coefficient k_{dc}. Porosity and permeability were prescribed based on the experimental observations. The advection–dispersion equation was coupled with the first order attachment-detachment kinetics, and solved using the internal HYDRUS-1D optimization routine. Aggregation and clogging were not considered based on the experimental observations discussed above. Straining of the NPs was also considered to be negligible and not included in the model because the ratio of the particle diameter to the median pore diameter was less than the threshold for straining (0.005) (Bradford et al., 2004).

Modeling was first performed assuming a homogeneous pore structure with an average connected porosity of 0.203. Flow parameters were evaluated by fitting the concentration data of slice 15 (the outlet) between 0 and 120 min – similar to a standard breakthrough curve (BTC) analysis, commonly adopted when spatial data are not available. Fig. 8 presents the experimental data and the fitted concentration results. Overall, using values of 0.16 mm^2/min, 0.018 min^{-1} and 0.07 min^{-1} for D, k_{ac} and k_{dc}, respectively, the simulation fits the experimental data, with a goodness-of-fit value (R^2) of 96.9% (Table 1).

To evaluate the extent to which the transport parameters derived following the standard BTC analysis can be applied to evaluate concentration evolution within the core, simulations were performed using the BTCs of four slices (slice 2, 5, 10, 14). These locations correspond to the centers of the four distinct porosity regions identified as Fig. 6. For these simulations, each region was assigned a unique set of hydraulic properties. The permeability was estimated from the average connected porosity of the region based on the Kozeny-Carman relationship. The transport parameters of the upstream region were first evaluated and used for the fitting of the transport parameters of the downstream region. Fig. 9 shows the simulation results for the four regions. While the goodness-of-fit values (R^2), ranging from 90.5% to 96.1% (Table 1), are not as high as for the homogeneous model, the improved performance

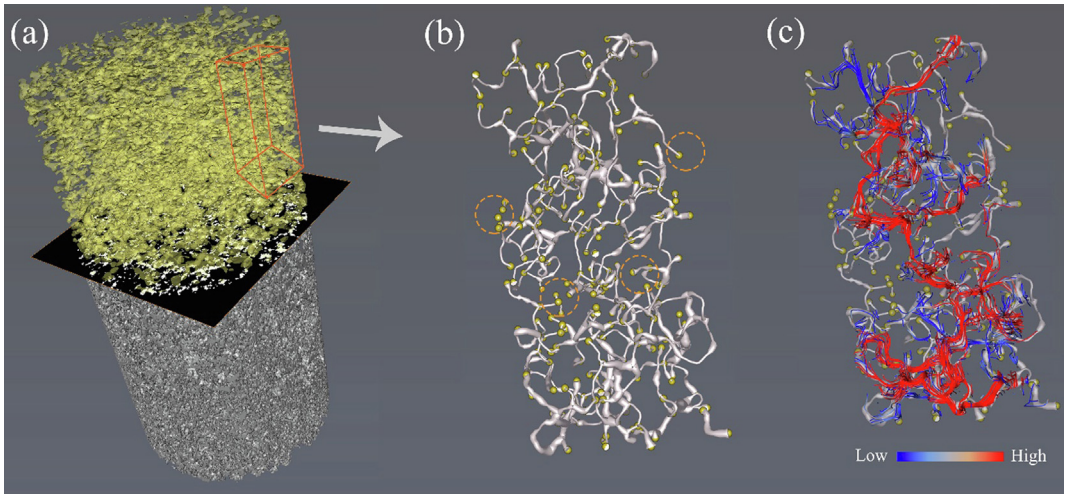

Fig. 7. Results of μCT imaging with (a) Volume rendering of the μCT segmented images with sandstone pores in yellow; (b) following binarisation to define the 3D skeleton for the highlighted subsection (see orange box) and showing nodes joined by capillary tubes, whose thickness are defined by the distance map; (c) Flow field shown as streamlines and color-coded according to relative fluid velocity (red:high velocity, blue:low velocity).

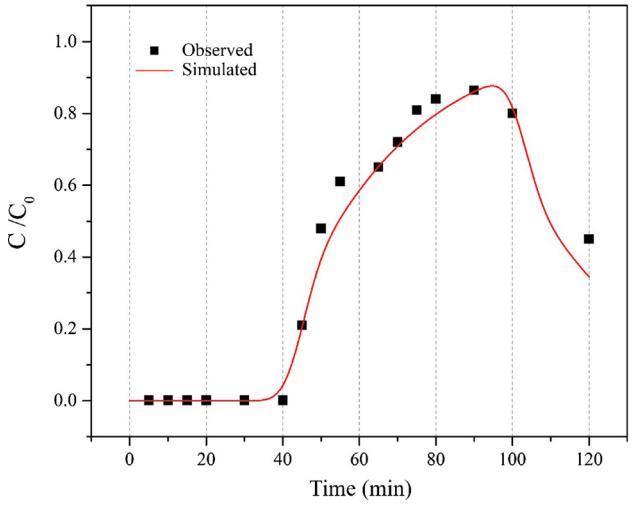

Fig. 8. Observed and simulated breakthrough curve of slice 15 (C is the measured concentration of iron, and C_0 is the influent iron concentration).

is highlighted by the low overall residual sum of squares, which are 0.114, 0.138, 0.074 and 0.041 for different slices. In contrast, using the transport parameters derived from the standard BTC analysis and assuming a homogeneous pore structure for the simulation of the local BTCs, the residual sum of squares is 0.276, 0.290, 0.328 and 0.044. The improved performance due to the consideration of spatial heterogeneity is most evident for region III. Transport parameters, k_{ac} and k_{dc} recovered from simulations, indicate the considerable impact of mechanical/electrostatic trapping and subsequent detachment of NPs on transport processes with respect to residual NPs. Comparing the performance of the two simulations further highlights the need of considering spatial heterogeneity. Nevertheless, some discrepancies between the experimental data and the simulations are observed principally in the tail of the concentration distribution in spite of identifying the attachment/detachment effects. This may result from the presence of dead-end pores, with this confirmed by the connectivity analysis completed using the Avizo visualization software. This effect cannot be accounted for in a purely 1D model.

The fitted parameters in different regions vary considerably, indicating the importance of spatial heterogeneity in controlling NP transport. In general, D and k_{dc} are smaller in the lower porosity region, whereas k_{ac} is larger (Table 1). Collectively, they result in reduced spreading and increased retention of the NPs. A higher attachment rate was observed in the lower permeability porous medium due to the effect of hydraulic conductivity and surface area (He et al., 2009).

These simulations demonstrate that although the standard BTC analysis with the assumption of homogeneity provides a reasonably good fitting for the overall transport process, it fails to capture concentration evolution within the core. This is the case, even though the degree of heterogeneity in the synthetic core sample used in our experiment is limited. Thus, the impacts of increased local heterogeneity are expected to be even more significant in natural heterogeneous systems, and to be important when regions of certain hydraulic properties need to be targeted. The spatial–temporal data measured using the SE-SPI sequences provide necessary information to investigate spatial heterogeneity and to quantify advection, dispersion and attachment/detachment mechanisms and their controls on the fate of colloidal particles in structured heterogeneous porous media.

Overall the SE-SPI sequences of low-field NMR provide an effective method to monitor the transport process of nanoparticles in rocks. Given its high resolution, this method may also be applied to low permeability geomaterials, e.g., carbonates and shales. However, some limitations of the technique should be noted. First, the relaxivity of paramagnetic NPs is the key parameter to quantify concentrations from NMR data. The calibration of relaxivity may be affected by the presence of paramagnetic substances with local magnetic field fluctuations, which may be the case in granites. Second, the NMR data provided by this method are the spectra representing multiple slices of defined thickness. The spatial resolution of data therefore depends on the number of slices set for the SE-SPI sequences but signal-to-noise ratio decreases as the number of subdivided slices increases.

5. Conclusions

For the first time, this study used SE-SPI sequences based on low-field NMR to successfully monitor the transport of modified nZVI particles in a consolidated sandstone. The ability of SE-SPI to simultaneously monitor multiple profiles along the core allows non-invasive observation of the transport of paramagnetic NPs. Iron concentrations were recovered, through the relaxivity constant, from the direct inversion of the spatio-temporal data. This study contributes an improved understanding of NP mobility in porous media to illuminate the important impacts of spatial heterogeneity on transport processes – *via* cross-confirmation using simulations and μCT imaging.

Experimental observations, including (i) the more rapid migration of the front, first detected at 15 mins, relative to bulk transport of the injected solution of NPs and (ii) the retention of NPs, with 27% of the iron retained at the conclusion of deionized water flushing, highlight the important controls of complex pore structure on the resulting retardation, attenuation and efflux of NPs.

Complementary numerical simulations evaluate sample heterogeneity and its effects on local transport properties. Transport parameters are inverted from the concentration data using two set of simulations and are compared to consider the impacts of spatial heterogeneity. In general, the model considering four regions of distinct porosities shows improved performance, as highlighted by the low overall residual sum of squares (0.041 to 0.138), compared to another model assuming a homogeneous pore structure (0.044 to 0.328). In addition, results show that the spatial heterogeneity of the transport and retention properties correlate with the pore structure extracted from μCT imaging. Compared to the most connected region, colloid dispersion (D) reduced from 0.20 to 0.10 cm^2/min, while the attachment (k_{ac}) increased from 0.007 to 0.025 min^{-1} in the lowest porosity region. The presence of well-connected flow paths and poorly-connected or dead-end pores in the sandstone results in tailing of the breakthrough curve and leads to discrepancies between experimental observations and results from equivalent-medium simulations.

In conclusion, SE-SPI sequences using low-field NMR is a promising

Table 1
Properties of sandstone and fitted parameters for NP transport.

Pore structure		Average porosity	Fitted transport parameters			
			D (cm^2/min)	k_{ac} (min^{-1})	K_{dc} (min^{-1})	R^2 (%)
Homogeneity		0.203	0.16	0.018	0.07	96.9
Heterogeneity	Inlet-slice 3	0.257	0.20	0.007	0.06	95.3
	Slice 3-slice 6	0.228	0.18	0.012	0.06	90.5
	Slice 6-slice 13	0.183	0.10	0.025	0.04	92.9
	Slice 13-outlet	0.196	0.15	0.015	0.08	96.1

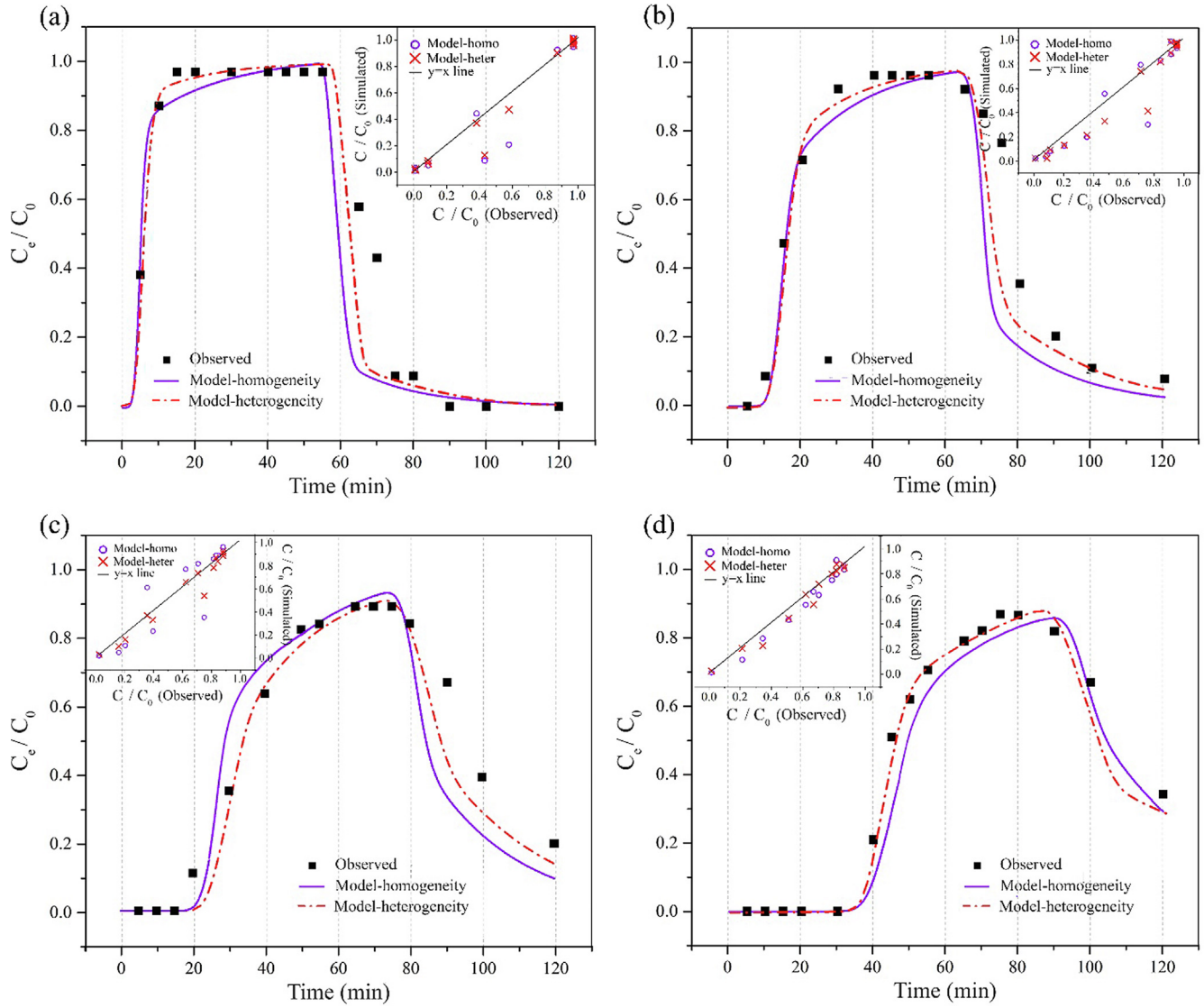

Fig. 9. Breakthrough curves of simulations for four slices compared to observed data for: (a) Slice 2; (b) Slice 5; (c) Slice 10; and (d) Slice 14. The insets are scatter plots to highlight the discrepancies between simulations and observations. Purple symbols and lines denote simulations assuming homogeneity, red symbols and lines denote simulations assuming heterogeneity with experimental observations as black symbols.

approach for characterization of the transport, retardation and attenuation of NPs in heterogeneous porous media even in the presence of nano-scale pores. In particular, and distinct from other NMR imaging methods, SE-SPI enables characterization at high-resolution. 2D or 3D models may be adopted in the future to consider the true impact of spatial-dimension on NP transport.

CRediT authorship contribution statement

Qian Zhang: Conceptualization, Methodology, Software, Formal analysis, Data curation, Writing - original draft. **Yanhui Dong:** Conceptualization, Methodology, Validation, Resources, Writing - review & editing, Funding acquisition. **Hang Deng:** Conceptualization, Validation, Investigation, Writing - review & editing. **Derek Elsworth:** Validation, Writing - review & editing.

Declaration of Competing Interest

The authors declare that they have no known competing financial interests or personal relationships that could have appeared to influence the work reported in this paper.

Acknowledgment

The research is financially supported by the Beijing Natural Science Foundation (Grant No. 8162042). Partial support was also provided by the Youth Innovation Promotion Association CAS (Grant No. 2016063). We are grateful to Dr. Cheng Gu at Nanjing University for providing the modified nZVI particles.

References

Zhang, W., 2003. Nanoscale iron particles for environmental remediation: an overview. J. Nanopart. Res. 5, 323–332.
Kanel, S.R., Greneche, J.M., Choi, H., 2006. Arsenic (V) removal from groundwater using nano scale zero-valent iron as a colloidal reactive barrier material. Environ. Sci. Technol. 40, 2045–2050.
Kocur, C.M., O'Carroll, D.M., Sleep, B.E., 2013. Impact of nZVI stability on mobility in porous media. J. Contam. Hydrol. 145, 17–25.
Karn, B., Kuiken, T., Otto, M., 2009. Nanotechnology and in situ remediation: a review of the benefits and potential risks. Environ. Health Persp. 117, 1823–1831.
Hosseini, S.M., Ataie-Ashtiani, B., Kholghi, M., 2011. Nitrate reduction by nano-Fe/Cu particles in packed column. Desalination 276, 214–221.
O'Carroll, D., Sleep, B., Krol, M., et al., 2013. Nanoscale zero valent iron and bimetallic particles for contaminated site remediation. Adv. Water Resour. 51, 104–122.
Phenrat, T., Saleh, N., Sirk, K., et al., 2007. Aggregation and sedimentation of aqueous

nanoscale zerovalent iron dispersions. Environ. Sci. Technol. 41, 284–290.
Tiraferri, A., Chen, K.L., Sethi, R., et al., 2008. Reduced aggregation and sedimentation of zero-valent iron nanoparticles in the presence of guar gum. J. Colloid Interface Sci. 324.
Tiraferri, A., Sethi, R., 2009. Enhanced transport of zerovalent iron nanoparticles in saturated porous media by guar gum. J. Nanopart. Res. 11, 635.
He, F., Zhao, D., Paul, C., 2010. Field assessment of carboxymethyl cellulose stabilized iron nanoparticles for in situ destruction of chlorinated solvents in source zones. Water Res. 44, 2360–2370.
Zhao, X., Liu, W., Cai, Z., et al., 2016. An overview of preparation and applications of stabilized zero-valent iron nanoparticles for soil and groundwater remediation. Water Res. 100, 245–266.
Fajardo, C., Costa, G., Nande, M., et al., 2019. Heavy metals immobilization capability of two iron-based nanoparticles (nZVI and Fe3O4): soil and freshwater bioassays to assess ecotoxicological impact. Sci. Total Environ. 656, 421–432.
Saif, S., Tahir, A., Chen, Y., 2016. Green synthesis of iron nanoparticles and their environmental applications and implications. Nanomaterials 6, 209.
Yoon, H., Pangging, M., Jang, M.H., et al., 2018. Impact of surface modification on the toxicity of zerovalent iron nanoparticles in aquatic and terrestrial organisms. Ecotoxicol. Environ. Saf. 163, 436–443.
Kim, S.C., Harrington, M.S., Pui, D.Y.H., 2007. Experimental study of nanoparticles penetration through commercial filter media. J. Nanopart. Res. 9, 117–125.
Vecchia, E.D., Luna, M., Sethi, R., 2009. Transport in porous media of highly concentrated iron micro-and nanoparticles in the presence of xanthan gum. Environ. Sci. Technol. 43, 8942–8947.
Phenrat, T., Kim, H.J., Fagerlund, F., et al., 2009. Particle size distribution, concentration, and magnetic attraction affect transport of polymer-modified Fe0 nanoparticles in sand columns. Environ. Sci. Technol. 43, 5079–5085.
Werth, C.J., Zhang, C., Brusseau, M.L., et al., 2010. A review of non-invasive imaging methods and applications in contaminant hydrogeology research. J. Contam. Hydrol. 113, 1–24.
Zinn, B., Meigs, L.C., Harvey, C.F., et al., 2004. Experimental visualization of solute transport and mass transfer processes in two-dimensional conductivity fields with connected regions of high conductivity. Environ. Sci. Technol. 38, 3916–3926.
Willingham, T.W., Werth, C.J., Valocchi, A.J., 2008. Evaluation of the effects of porous media structure on mixing-controlled reactions using pore-scale modeling and micromodel experiments. Environ. Sci. Technol. 42, 3185–3193.
Turner, M.L., Knuefing, L., Arns, C.H., et al., 2004. Three-dimensional imaging of multiphase flow in porous media. Physica A. 339, 166–172.
Nizovtsev, M.I., Stankus, S.V., Sterlyagov, A.N., et al., 2008. Determination of moisture diffusivity in porous materials using gamma-method. Int. J. Heat Mass Transf. 51, 4161–4167.
Peng, S., Hu, Q., Dultz, S., et al., 2012. Using X-ray computed tomography in pore structure characterization for a Berea sandstone: resolution effect. J. Hydrol. 472, 254–261.
Ramanan, B., Holmes, W.M., Sloan, W.T., et al., 2011. Investigation of nanoparticle transport inside coarse-grained geological media using magnetic resonance imaging. Environ. Sci. Technol. 46, 360–366.
Bray, J.M., Lauchnor, E.G., Redden, G.D., et al., 2017. Impact of mineral precipitation on flow and mixing in porous media determined by microcomputed tomography and MRI. Environ. Sci. Technol. 51, 1562–1569.
Lehoux, A.P., Faure, P.,Michel, E, et al., 2017. Transport and adsorption of nano-colloids in porous media observed by magnetic resonance imaging. Transport Porous Med. 119, 403–423.
Lakshmanan, S., Holmes, W.M., Sloan, W.T., et al., 2015. Characterization of nanoparticle transport through quartz and dolomite gravels by magnetic resonance imaging. Int. J. Environ. Sci. Technol. 12, 3373–3384.
Mitchell, J., Fordham, E.J., 2015. Contributed review: nuclear magnetic resonance core analysis at 0.3 T. Rev. Sci. Instrum. 85, 111502.
Mitchell, J., Chandrasekera, T.C., Johns, M.L., et al., 2010. Nuclear magnetic resonance relaxation and diffusion in the presence of internal gradients: the effect of magnetic field strength. Phys. Rev. E. 81, 026101.
Petrov, O.V., Ersland, G., Balcom, B.J., 2011. T2 distribution mapping profiles with phase-encode MRI. J. Magn. Reson. 209, 39–46.
Jia, H., Gu, C., Boyd, S.A., et al., 2011. Comparison of reactivity of nanoscaled zero-valent iron formed on clay surfaces. Soil Sci. Soc. Am. J. 75, 357–364.
Gu, C., Jia, H., Li, H., et al., 2010. Synthesis of highly reactive subnano-sized zero-valent iron using smectite clay templates. Environ. Sci. Technol. 44, 4258–4263.
Jia, H.Z., Wang, C.Y., 2013. Comparative studies on montmorillonite-supported zero-valent iron nanoparticles produced by different methods: reactivity and stability. Environ. Technol. 34, 25–33.
Xie, H.J., Li, A.F., Qin, J.F. et al., 2016. Manufacture of water wet artificial core by chemical modification method. In: International Symposium of the Society of Core Analysts held in Snowmass, Colorado, USA.
Pykett, I.L., Newhouse, J.H., Buonanno, F.S., et al., 1982. Principles of nuclear magnetic resonance imaging. Radiology 143, 157–168.
Caravan, P., Ellison, J.J., Mcmurry, T.J., et al., 1999. Gadolinium(III) chelates as MRI contrast agents: structure, dynamics, and applications. Chem. Rev. 99, 2293.
Bloembergen, N., Morgan, L.O., 1961. Proton relaxation times in paramagnetic solutions. effects of electron spin relaxation. J. Chem. Phys. 34, 842–850.
Strijkers, G.J., Mulder, W.J., van Tilborg, G.A., et al., 2007. MRI contrast agents: current status and future perspectives. Anticancer Agents Med Chem. 7, 291–305.
Behroozmand, A.A., Keating, K., Auken, E., 2014. A review of the principles and applications of the NMR technique for near-surface characterization. Surv. Geophys. 36, 27–85.
Šimůnek, J., He, C., Pang, L., et al., 2006. Colloid-facilitated solute transport in variably saturated porous media. Vadose Zone J. 5, 1035–1047.
Bradford, S.A., Bettahar, M., Šimůnek, J., et al., 2004. Straining and attachment of colloids in physically heterogeneous porous media. Vadose Zone J. 3, 384–394.
He, F., Zhang, M., Qian, T.Q., et al., 2009. Transport of carboxymethyl cellulose stabilized iron nanoparticles in porous media: column experiments and modeling. J. Colloid Interface Sci. 334, 96–102.